

# Spatially Heterogeneous Chlorine Incorporation in Organic–Inorganic Perovskite Solar Cells

Yanqi Luo,<sup>†</sup> Shany Gamliel,<sup>‡</sup> Sally Nijem,<sup>‡</sup> Sigalit Aharon,<sup>‡</sup> Martin Holt,<sup>§</sup> Benjamin Stripe,<sup>||</sup> Volker Rose,<sup>§,||</sup> Mariana I. Bertoni,<sup>⊥</sup> Lioz Etgar,<sup>‡</sup> and David P. Fenning<sup>\*,†</sup>

<sup>†</sup>Department of Nanoengineering, University of California San Diego, La Jolla, California 92093, United States

<sup>‡</sup>The Hebrew University of Jerusalem, Institute of Chemistry, Casali Center for Applied Chemistry, Jerusalem, 91904, Israel

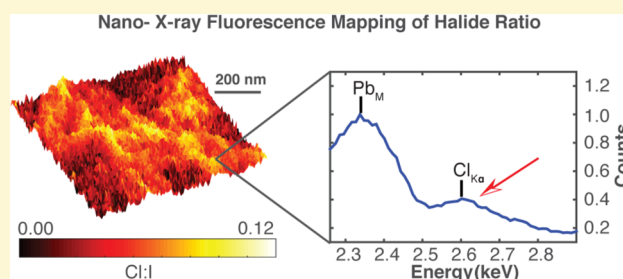
<sup>§</sup>Center for Nanoscale Materials, Argonne National Laboratory, Argonne, Illinois 60439, United States

<sup>||</sup>Advanced Photon Source, Argonne National Laboratory, Argonne, Illinois 60439, United States

<sup>⊥</sup>School of Electrical, Computer and Energy Engineering, Arizona State University, Tempe, Arizona 85287, United States

## Supporting Information

**ABSTRACT:** Spatial heterogeneities in the chemical makeup of thin film photovoltaic devices are pivotal in determining device efficiency. We report the in-plane spatial distribution and degree of chlorine incorporation in organic–inorganic lead halide perovskite absorbers by means of nondestructive synchrotron-based nanoprobe X-ray fluorescence. The presence of chlorine is positively identified in  $\text{CH}_3\text{NH}_3\text{PbI}_3$  films synthesized with Cl-containing precursors and as an impurity in some films synthesized with nominally Cl-free precursors. The impurity may be introduced from precursors or as contaminants during film synthesis. The films formed from Cl-containing precursors contain roughly an order of magnitude higher amount of chlorine, with Cl:I values greater than 0.02 found whether Cl is present in either the organic or the inorganic precursor for both one- and two-step fabrication processes. A spatial variation in the Cl incorporation is observed within single particles and as well as between particles within a given film, and the standard deviation of the Cl:I ratio across the films is up to 30% of the average value. Understanding and controlling the heterogeneous distribution of chlorine in hybrid perovskite layers may offer a path to improve their photovoltaic performance.



## INTRODUCTION

The rapid development of solid-state organometal halide perovskite solar cells has garnered significant attention to the relationship between their hybrid chemistry and their exceptional optoelectronic properties<sup>1–3</sup> that could enable wide-ranging potential applications.<sup>4–7</sup> The power conversion efficiency of perovskite solar cells has risen to above 22% (independently certified) with extensive optimization of film properties and device architectures.<sup>8–12</sup> The performance of this organic–inorganic halide cell is related to the optoelectronic properties of the organic lead halide absorber layer, most commonly  $\text{CH}_3\text{NH}_3\text{PbX}_3$  ( $X = \text{I}$  and  $\text{Br}$ ), and can be influenced by chemical composition, film morphology, and device architecture.<sup>7,13–17</sup> Recent reports have shown that using chloride containing salts or precursors (methylammonium chloride,  $\text{MACl}$ , and/or  $\text{PbCl}_2$ ) can assist perovskite crystal growth because chloride ions or the formation of  $\text{PbCl}_2$  nanocrystals (in a one-step deposition) can act as a nucleation center<sup>11,18</sup> due to size of Cl and  $\text{PbCl}_2$  solubility. Additionally, the presence of  $\text{MACl}$  can also enhance the adsorption of lead iodide perovskite absorber on the  $\text{TiO}_2$  substrate and produce large oriented crystallite domains by allowing slow crystal growth.<sup>18,19</sup>

In perovskite solar cell synthesis, during the final annealing step the majority of the chlorine sublimates, resulting in a low degree of chlorine incorporation.<sup>20</sup> A number of reports with varying film preparations have failed to identify Cl incorporation with X-ray photoelectron spectroscopy (XPS) or energy dispersive X-ray spectroscopy (EDS),<sup>21–23</sup> although bulk incorporation of chlorine as  $\text{CH}_3\text{NH}_3\text{PbI}_{3-x}\text{Cl}_x$  with  $x < 0.4$  has been shown by benchtop X-ray fluorescence, synchrotron-based X-ray absorption spectroscopy, and photothermal induced resonance (PTIR).<sup>20,24–26</sup> X-ray absorption near-edge spectroscopy indicates that remnant Cl cannot be fully explained by the chemical state of Cl found in  $\text{MACl}$  and  $\text{PbCl}_2$  precursors.<sup>25</sup> More typically, chlorine incorporation has been measured to be between  $0.030 < x < 0.41$  by XPS or EDS.<sup>27</sup>

Minor element incorporation in semiconductor absorbers typically leads to detrimental introduction of trap states in the bandgap,<sup>28,29</sup> although at times it can be beneficial. For example, Na incorporation has been shown to provide beneficial passivation of grain boundaries in CIGS solar

Received: May 23, 2016

Revised: August 30, 2016

Published: August 30, 2016

Table 1. Effect of Precursor and Deposition Method on Cl Incorporation of Perovskite Samples

	precursors	Cl:I mass ratio	
		mean	$C_v$
precursors with Cl	PbI <sub>2</sub> + MACl:MAI (2:1, 2s)	0.062 (0.02)	0.29
	PbI <sub>2</sub> + MACl:MAI (1:1, 1s)	0.030 (0.01)	0.33
	PbCl <sub>2</sub> + MAI (1s)	0.027 (0.01)	0.32
precursors without Cl	PbI <sub>2</sub> + MAI ( <i>Spray</i> )	0.0058 (0.002)	0.30
	PbI <sub>2</sub> + MAI (1s)	0.0013 (0.002)	1.2

cells,<sup>30</sup> and H is used to passivate structural defects in silicon solar cells.<sup>31</sup> Photoluminescence and EDS measurements have tentatively correlated chlorine with improved electronic performance, although its distribution in the film remains poorly quantified.<sup>7</sup>

In this study, we use synchrotron-based nanoprobe X-ray fluorescence (XRF) microscopy to measure the nanoscale in-plane spatial distribution of chlorine in perovskite solar cells. Nano-XRF is a nondestructive X-ray technique with large penetration depth such that it can measure through film layers with high elemental specificity and a ppm detection limit. By mapping the elemental distribution in nominally methylammonium lead iodide films with 100 nm spatial resolution, we find that chlorine is incorporated heterogeneously across the film, varying between individual particles. We quantify the variation in local incorporation of chlorine among different fabrication methods and find that it is largely independent of whether the Cl containing precursor is the organic or the inorganic component. All perovskite film stacks studied here are fabricated under standard conditions except no hole-transport layer is present.<sup>32</sup> Such a structure has been shown to produce a range of 10.8 to 12.8% efficiency<sup>33–35</sup> and allows a stronger XRF response to be measured through a largely transparent Au back contact without the intervening hole-transport layer. The XRF nanoprobe provides insight into not only the local chemical stoichiometry of organometal halide but also the chemical distribution within this thin film system. The nanoprobe fluorescence data reveal a microscopically heterogeneous distribution of chlorine and its manipulation by perovskite precursor chemistry, opening new directions toward understanding how the distribution can be harnessed to optimize and stabilize hybrid perovskite solar cells.

## EXPERIMENTAL SECTION

**Materials.** Methylammonium iodide (MAI) was prepared and synthesized following a previously published method<sup>16,36</sup> using methylamine (MA, 40% in methanol, TCI) and hydriodic acid (HI, 57% in water, Sigma-Aldrich). Methylammonium chloride (MACl) was obtained via the same synthesis route but with hydrochloric acid (HCl, 37% in water, Sigma-Aldrich). Typically, a 1.2:1 molar ratio of methylamine and hydriodic acid were used to form MAI crystals and 1.7:1 molar ratio of methylamine and hydrochloric acid were used to obtain MACl crystals. To study the mix-halide system, a mixture of MACl:MAI with a molar ratio of 1:2 was prepared in isopropanol. Besides the organic halide crystals, PbI<sub>2</sub> (powder, 99% Sigma-Aldrich) and PbCl<sub>2</sub> (powder, 98% Sigma-Aldrich) were used as-received for precursors.

**Device Fabrication.** A series of solar cell thin film stacks was fabricated utilizing three different deposition methods: one-step (1s), two-step (2s),<sup>37</sup> and *spray* deposition<sup>38</sup> with various ratios of methylammonium halide and inorganic precursors to produce perovskite absorbers on a mesoporous and a dense layer of TiO<sub>2</sub> substrate for both 1s and 2s method, and planar TiO<sub>2</sub> for *spray* deposition method (detailed compositions in Table 1). In the 1s method, perovskite solution (40 wt % in DMF) was deposited onto

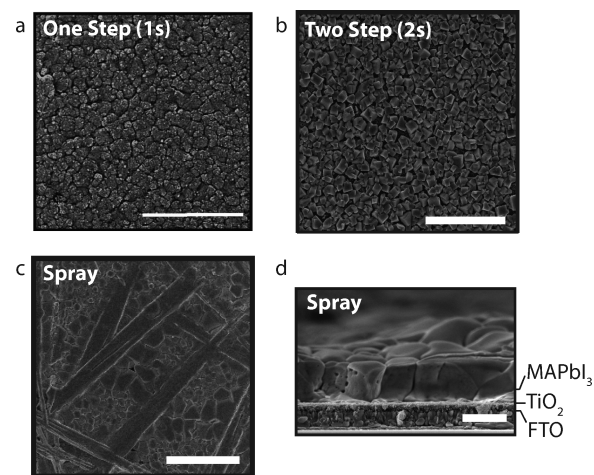
the mesoporous TiO<sub>2</sub> by spin-coating at 2000 rpm, followed by an anneal at 90 °C for 30 min. For the 2s deposition method, PbI<sub>2</sub> was first spin-coated on mesoporous TiO<sub>2</sub> at 2000 rpm for 25 s, allowed to stabilize for 3 min, then annealed at 70 °C for 30 min. Second, this layer is dipped into methylammonium halide solution for 20s and then annealed at 90 °C for 30 min to form the active perovskite absorber layer. These spin velocity, annealing temperature and time, dipping time, and precursor concentration parameters have been established as optimal for the hole transport layer-free solar cell architecture used here.<sup>37</sup> *Spray* deposition used the same perovskite solution concentration as the 1s method but used DMF as the solvent. The solution was sprayed using a Paasche H-SET airbrush onto a planar TiO<sub>2</sub> substrate held at 80 °C. The deposited layer was then annealed at 80 °C for 40 min. The 40 nm Au back contact layer was evaporated over the perovskite layer under  $5 \times 10^{-6}$  Torr.

Table 1 details the samples that were investigated, the ratios of their precursor chemistry, and their average chlorine incorporation as measured by nano-XRF and described below. The samples are grouped into two different categories, those with Cl-containing precursors and those with nominally Cl-free precursors.

The spatial average of the Cl:I ratio, its standard deviation (in parentheses), and its coefficient of variation  $C_v$  ( $\sigma/\mu$ ) for each sample is obtained by analyzing the Cl:I maps (see below).

An FEI Magellan UHR Scanning Electron Microscope (SEM) was used to study the film morphology. Film stacks with chemistries identical to those investigated by X-ray fluorescence were exposed at 5–10 keV at various magnifications.

Scanning electron microscopy reveals significant changes in grain morphology dependent upon deposition method (Figure 1), in agreement with previous demonstrations of the syntheses.<sup>6,38,39</sup> Smaller crystal domain regions are observed for both 1s and 2s deposition technique than *spray* deposition method. The film thickness is around 300 nm when using 1s and 2s deposition methods.



**Figure 1.** SEM images of MAPbI<sub>3</sub> deposited via (a) one-step deposition (1s, scale bar 5 μm) (b) two-step deposition (2s, scale bar 5 μm) (c) *spray* deposition (scale bar 10 μm) (d) A cross-section of a *spray*-deposited sample on TiO<sub>2</sub> and the F:SnO<sub>2</sub> substrate (scale bar 1 μm).

Spray deposition, in particular, produces significantly larger grain sizes including needle-like grains of up to about  $30\ \mu\text{m}^2$ . In addition, the grain boundaries are largely vertical reaching through the depth of the film with film thickness around  $1.0\ \mu\text{m}$  for the spray film stack (Figure 1d).

**Synchrotron-Based Characterization.** The perovskite films were studied by synchrotron-based nanoprobe X-ray fluorescence (XRF) at beamline 26-ID-C of the Advanced Photon Source and Center for Nanoscale Materials at Argonne National Laboratory to characterize the elemental distribution in the materials. The Hard X-ray Nanoprobe uses two collinear undulators and zone plate optics to enable fluorescence analysis of major and minor elemental constituents in a focused beam down to  $30\ \text{nm}$  fwhm.<sup>40</sup> The zone plates used in this study achieved a  $90\ \text{nm}$  fwhm (see Figure S1 of the Supporting Information, SI). The sub- $100\ \text{nm}$  beam, when stepped finely, can see even smaller features (e.g.,  $30\ \text{nm}$  features) but at a loss of fidelity relative to optimum contrast. Figure 2a illustrates the experimental

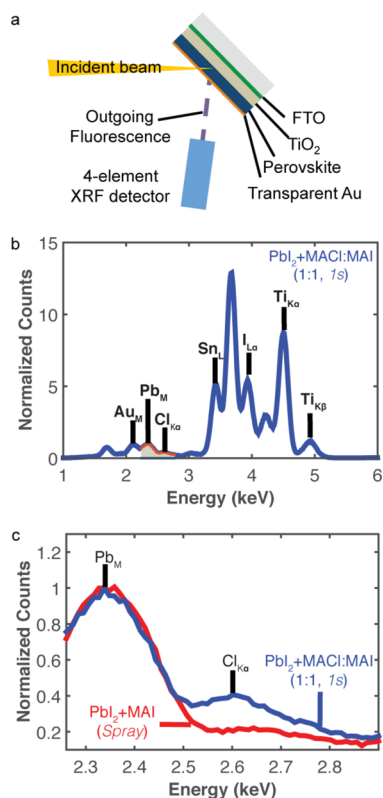


**Figure 2.** (a) Backside X-ray illumination and fluorescence detection through the transparent Au layer is used to probe elemental distributions in perovskite thin film stacks. A nanopositioning stage moves the sample in front of the focused X-ray beam producing a X-ray fluorescence map. (b) A typical single-point X-ray fluorescence spectrum revealing that, in addition to detecting all major elements in the film stack, Cl is positively identified (c) The normalized fluorescence spectrum in the 2260–2900 eV range (shaded area of (b)) containing the Cl  $K\alpha$  emission. Two samples are compared, one with Cl-containing organic precursors that shows Cl is present and one made with Cl-free precursors with no Cl detected.

setup for the photon-in, photon-out XRF measurement. From the XRF spectrum, we identify the elements in the film according to their characteristic fluorescence energy. In the experimental setup used here, the attenuation length is  $11.5\ \mu\text{m}$  in  $\text{CH}_3\text{NH}_3\text{PbI}_3$  at the  $10\ \text{keV}$  incident X-ray energy.<sup>41</sup> Due to the large attenuation length, the collected signal response is a result of fluorescence from the entire thickness of the film.

Using the nanopositioning stages of the hard X-ray nanoprobe, we rastered the focused X-ray beam over the sample with a step size as

small as  $25\ \text{nm}$  to construct high-resolution maps of typically  $5 \times 5\ \mu\text{m}^2$  with  $1\ \text{s}$  dwell/pt. With the step size smaller than the X-ray beam's fwhm, the film stack is oversampled to ensure the spatial fidelity of the signal response and avoid spatial aliasing effects. A fluorescence image is constructed for elements of interest by combining the signal response from the four-element energy dispersive detector, fitting the elemental peak and removing contributions from the spectral background.<sup>42</sup> RF-8<sup>43</sup> X-ray fluorescence thin film reference materials were used to quantify the XRF spectra, and the MAPS software<sup>44</sup> was used to fit and deconvolute the elemental peaks in the fluorescence data set, with particular attention paid to the fit in the low-energy region where the Cl  $K\alpha$  is found. The XRF maps were corrected to account for the attenuation of the incident beam and exiting fluorescence through the gold layer and the film under the assumption of uniform thickness and homogeneous perovskite composition as a function of depth (see SI section 1.4 for details).

## RESULTS AND DISCUSSION

A typical single-point XRF measurement is shown in Figure 2b indicating the detection of Pb, I, and Cl in a  $\text{PbI}_2$ +MAI:MAI film. Au from the semitransparent back contact, Ti from the underlying mesoporous  $\text{TiO}_2$  and blocking layer, and Sn from the  $\text{SnO}_2$ :F substrate are also detected (Figure 2a). Figure 2c magnifies the shaded area indicated in Figure 2b. It compares the  $\text{PbI}_2$ +MAI:MAI sample, made with Cl-containing precursors, to another sample made with Cl-free precursors and positively identifies the presence of chlorine in the sample made with Cl-containing precursors, indicated by the Cl  $K\alpha$  emission at  $2.62\ \text{keV}$ . While readily identifiable, the signal response of Cl  $K\alpha$  indicates that only trace amounts of chlorine remain in the system.

The spatial distribution and chemical composition of the perovskite films were found to be stable on the  $\sim 100\ \text{nm}$  length scale during the repetitive mapping of the focused  $10\ \text{keV}$  X-ray beam with  $4 \times 10^8$  photons/sec (Figure S3). Note that a stable composition in the nano-XRF measurement does not necessarily indicate *electronic* stability under the X-ray beam. However, no systematic changes in the *elemental* distributions are observed upon measuring the same area of sample three times consecutively ( $\sim 3\ \text{h}$  under X-ray illumination).

**Cl Incorporation is Tuned by Cl Content of Precursors.** We find that using chlorine-containing organic or inorganic precursors results in a significant chlorine incorporation into the hybrid perovskite films. No remnant MAI or  $\text{PbCl}_2$  is observable by benchtop X-ray diffraction in any of these films (Figure S2). Trace chlorine impurities are detected in some samples produced with nominally Cl-free precursors. Five different organic and inorganic precursor combinations and deposition methods are analyzed using Nano-XRF and are shown in Figure 3. The XRF maps in Figure 3 are organized in descending order of average Cl:I mass ratio measured in the samples. The first three samples, containing the higher average Cl:I ratios, are the cells fabricated using either the Cl-containing organic halide MAI (row 1 and row 2) or the Cl-containing precursor  $\text{PbCl}_2$  (row 3). Row 1 shows the XRF data for the Cl-containing film synthesized by the two-step method with 2:1 MAI:MAI. Row 2 shows the data for a one-step film with 1:1 MAI:MAI. The two bottom rows show the nominally Cl-free samples synthesized with  $\text{PbI}_2$  and MAI with different depositing methods spray (row 4) and 1s (row 5). For a given sample, the Pb and I maps (Figure 3a and b, e and f, i and j, m and n, and q and r) show similar spatial elemental distribution. This covarying distribution of Pb and I



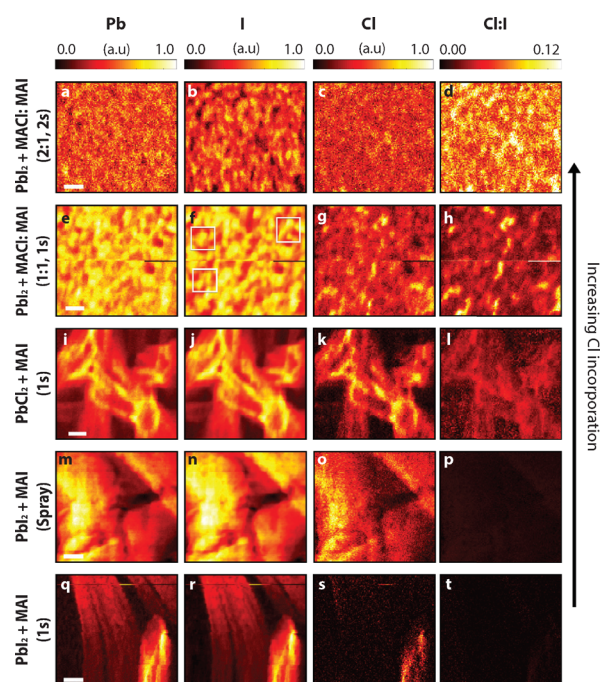


**Figure 3.** Chemical heterogeneity within hybrid perovskite films: Lead, iodine, and chlorine and Cl:I mass ratio X-ray fluorescence maps (1  $\mu\text{m}$  scale bars). Maps are corrected to account for incident beam and outgoing fluorescence attenuation through the multiple layers. XRF images are arranged in descending order of average Cl:I ratio response. The quantitative Cl:I mass ratio, defined at each point as the measured chlorine loading in  $\mu\text{g}/\text{cm}^2$  over the iodine loading in  $\mu\text{g}/\text{cm}^2$ . Cl:I ratio maps are scaled identically from 0.00 to 0.12 for all samples.

major components indicates the boundaries of the perovskite particles (cf. Figures 1 and 3).

The Cl elemental distribution depends strongly on the film precursors. A normalized Cl XRF map and the quantitative Cl:I ratio are shown for each sample to support detailed comparisons between samples. All halide maps are scaled to their individual maximum for comparison of the relative distributions across samples in Figure 3. The quantitative data without normalization are shown in Figure S5. The Cl spatial distribution has a similar pattern as lead and iodine in the Cl-containing precursor samples, but close comparison reveals the Cl distribution is distinct. The Cl:I ratio maps are all scaled identically from 0 to 0.12 Cl:I. The ratio maps not only provide a local chemical halide composition ratio but show local variations in chlorine incorporation relative to iodine. The inhomogeneity of halide chemistry is clear in the ratio maps.

The Cl content of the resulting film can be directly manipulated by the amount of Cl-containing precursor used in the synthesis. When chlorine is intentionally present in the precursors (rows 1–3), the sample's Cl XRF image is bright across the film, indicating local Cl content is high (Figure 3c, g, and k). The  $\text{PbI}_2 + \text{MACl}:\text{MAI}$  (2:1, 2s) sample has the highest Cl-content in the precursors and subsequently the highest Cl:I ratio and the largest amount of chlorine rich areas (row 1). The Cl:I ratio map for the  $\text{PbI}_2 + \text{MACl}:\text{MAI}$  (1:1, 1s) reveals slightly higher local Cl:I ratios than the  $\text{PbCl}_2 + \text{MAI}$  and a greater variance as evidenced by larger contrast in the ratio map. Cl is incorporated whether it is present in the organic or the inorganic precursor.

An analysis of the area-averaged Cl:I ratio and its standard deviation for each precursor and deposition method demon-

strates that the degree of chlorine incorporation is affected by the amount of Cl introduced by precursors during perovskite crystal formation (graphically presented in Figure 4, tabulated

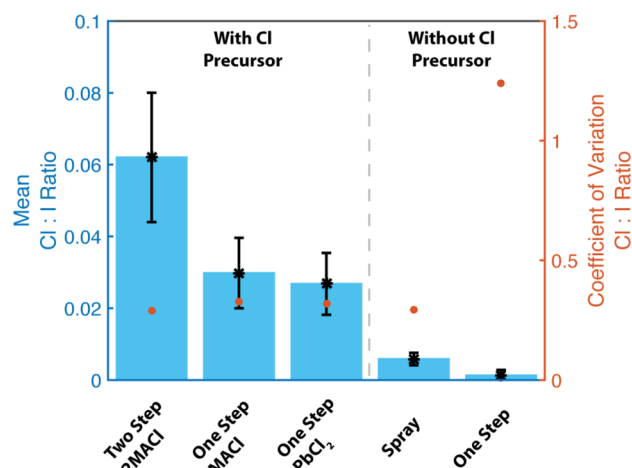


**Figure 4.** Effect of perovskite precursors on halide mass ratio. The blue bars indicate the average Cl:I mass ratio for each sample, the error bar shows the standard deviation, and the red dot is the coefficient of variation within samples. This set of plotted data is also summarized in Table 1.

in Table 1). This area-average elemental analysis is performed only over regions where the perovskite film covers the mesoporous and planar layer  $\text{TiO}_2$  and substrate (Figure S4). Figure 4 is categorized with films with Cl-containing precursors on the left and those with nominally-Cl free precursors on the right. When either  $\text{PbCl}_2$  or  $\text{MACl}$  are used as precursors, the final average Cl:I ratio lies in the range of  $0.027 < \text{Cl:I} < 0.062$ . Several reports have indicated a typical Cl content of 1–4%<sup>5,27</sup> in good agreement with the observation here of the highest average Cl:I ratio of 0.062 and its spatial standard deviation of 0.02 for the 2:1  $\text{MACl}:\text{MAI}$  sample. The other samples produced with Cl-containing precursors, one with a 1:1 ratio of  $\text{MACl}:\text{MAI}$  and the other using  $\text{PbCl}_2$ , have relatively similar Cl:I ratios of  $0.030 \pm 0.01$  and  $0.027 \pm 0.01$ , roughly half that of the sample prepared with 2:1  $\text{MACl}:\text{MAI}$ .

The high sensitivity of the nano-XRF instrument also allows us to determine chlorine contamination in several nominally Cl-free preparations, with Cl:I in a range of 0.0012 to 0.0058. This amount of chlorine incorporation may be due to process or precursor contamination. Of note, no chlorine was detectable in a number of similar measurements of  $\text{CH}_3\text{NH}_3\text{PbI}_3$  films (not shown) made with two- and one-step depositions with chlorine-free precursors.

In the nominally Cl-free precursor compositions where it is above detection limits, Cl incorporation is sparse (Figure 3o, s) and the local Cl:I ratio small relative to the Cl-containing precursor films (Figure 3c, g, and k). Both Cl:I ratio maps of the nominally Cl-free samples are almost black, especially Figure 3t, implying the degree of chlorine incorporation is small and highly localized where it does occur.

The nano-XRF data suggest that the degree of chlorine incorporation is dominated by the chlorine content of the precursors and that it is largely independent of whether chlorine-containing precursor is organic or inorganic component. While there may be some process dependence, for example the Cl:I ratio in the 2s sample (Figure 3c) is slightly narrower in distribution than the 1s preparations (Figure 3g

and k), the Cl:I ratio maps offer a clear indication that Cl is generally incorporated in these films in a highly heterogeneous distribution (see Figure S5 for Cl:I ratio maps of each sample with its own color scaling).

The coefficient of variation  $c_v$ , defined as the ratio of the standard deviation over the sample mean ( $\sigma/\mu$ ), can be used to compare the relative magnitude of the variation in Cl:I ratio between the deposition processes. In the one-step nominally Cl-free sample, the  $c_v$  is highest at 1.2, attributable to the presence of Cl only in a single particle within the measured area. In all other samples, the  $c_v$  fluctuates between 0.29 and 0.33 for the various organic and inorganic precursor and deposition methods, indicating that the processes all lead to a relatively large variation in Cl:I ratio across the sample. As hybrid perovskite materials are scaled up to larger film areas, the coefficient of variation in chemical composition determined by the deposition process may serve as a predictive metric of the batch variance in optoelectronic performance.

**Cl Heterogeneity between Particles within a Single Film.** To study Cl heterogeneity among individual particles, individual particles are identified from the iodine XRF maps manually. For each particle, a point-by-point analysis of the local Cl:I ratio within the particle is performed. Note that the boundaries of the particles identified may encompass multicrystalline regions themselves. However, the particle boundaries observed by nano-XRF correspond well to those observed in the SEM (Figure 1). The resulting distributions of Cl:I ratio within the individual particles are displayed in Figure 5 for the  $\text{PbI}_2 + \text{MACl}:\text{MAI}$  (1:1, 1s). In Figure 5, each boxplot represents the distribution of the halide ratio within an individual particle in the sample, sorted in order of increasing median Cl:I ratio. Each boxplot thus indicates the heterogeneity of Cl distribution within a given particle, while the variation between boxplots indicates the variation between the many particles measured in the film. The median Cl:I ratio in the particles within the single film varies by a factor of 2. In addition, the wide distribution of Cl:I stoichiometry within single particles shown in Figure 5 demonstrates that the overall Cl heterogeneity in a sample is the consequence of contributions from local Cl:I ratio variations within individual particles.

**Cl Heterogeneity within Single Particles.** The measured variation in Cl:I ratio within single particles can be as large as the variation across the film. Figure 6 details three particles randomly selected and highlighted in Figure 3f. For each particle an approximate particle boundary is determined from the I XRF map and indicated across the I, Cl, and Cl:I XRF maps. In the Cl maps of Figure 6b, e, and h, the inhomogeneous distribution of chlorine is revealed by readily visible chlorine-poor and -rich areas. The median halide ratio of the three regions are similar at 0.025, 0.024, and 0.030, respectively, but the Cl:I ratio within each particle varies by a factor of 4–6 $\times$  and the corresponding Cl:I histogram on the right-hand side indicates the overall distribution of the halide stoichiometry within the selected region. In particular, it is interesting to note that Cl rich regions are adjacent to the crystal region where Cl:I ratio is low.

The nano-XRF data provide evidence of a chlorine distribution that varies strongly within lead halide perovskite thin film materials, both between particles and among single particles. The overall Cl content detected here would correspond to a range from  $0 < x < 0.52$  were it incorporated in the perovskite lattice as  $\text{CH}_3\text{NH}_3\text{PbI}_{3-x}\text{Cl}_x$ , amounts similar

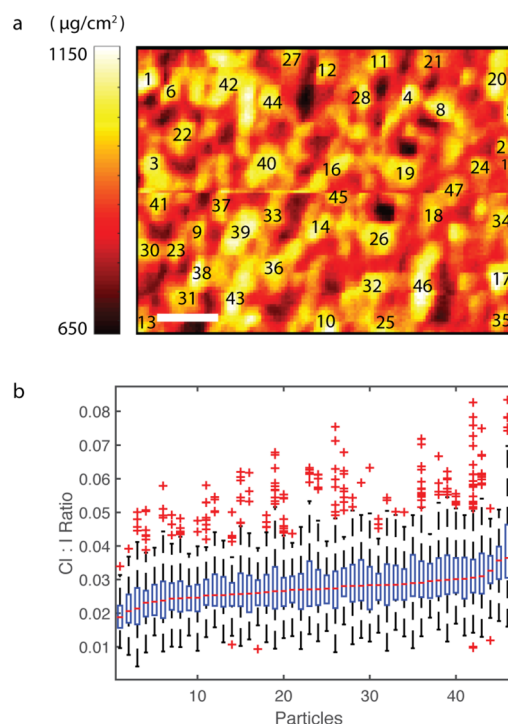


**Figure 5.** Analysis of local Cl:I mass ratio in individual particles. (a) Particles identified by algorithmic detection are shown indexed in the I map of the Cl-containing precursor sample  $\text{PbI}_2 + \text{MACl}:\text{MAI}$  (1:1, 1s) with 1  $\mu\text{m}$  scale bar. (b) Boxplots of the Cl:I distribution within each indexed particle. The red line within each boxplot is the median Cl:I ratio of the particle, and the box area represents the 25<sup>th</sup>–75<sup>th</sup> percentiles of the data set. The red crosses of each boxplot indicate what would typically be considered outliers (data beyond  $2.7\sigma$ , where  $\sigma$  is the standard deviation of individual particles). The particle index is listed on the abscissa. Among the particles analyzed, the median Cl:I ratio varies by nearly a factor of 2. The range within a single particle varies by more than a factor of 2.

to or greater than previous reports.<sup>5,45</sup> The large degree of variation of Cl distribution in the film may be partially contributed to by the presence of second phases, including heterogeneously distributed  $\text{PbCl}_2$  nanocrystal nucleation centers,<sup>18</sup> although none are not detected by benchtop XRD (Figure S2). While the XRD results are negative, we cannot completely rule out that some Cl remains as trace  $\text{MACl}$  or  $\text{PbCl}_2$  with the nano-fluorescence data set.

In general, the concentration of Cl within perovskite thin film layers decreases with extended annealing.<sup>20,26</sup> We note that the annealing used in this study was found to be optimal for HTL-free device performance,<sup>34</sup> despite being shorter and lower in temperature than that found optimal in other studies for HTL-containing devices (100  $^\circ\text{C}$ , 45 min).<sup>46</sup> However, the  $\text{MACl}$  in the precursors here is also more dilute to start when compared to previous study of remnant Cl incorporation.<sup>25</sup> Recent X-ray absorption spectroscopy by Pool et al.<sup>25</sup> also suggests that as annealing progresses the chemical environment of Cl takes on a more perovskite-like character. If the remnant Cl is indeed on the perovskite lattice, then the varying composition observed within single particles corroborates significant flexibility in the bulk chemistry and high tolerance in lattice strains.<sup>47</sup> Similar variations in composition within the same crystal structure have been found, for example, in the quaternary photovoltaic absorber CIGS.<sup>48</sup>

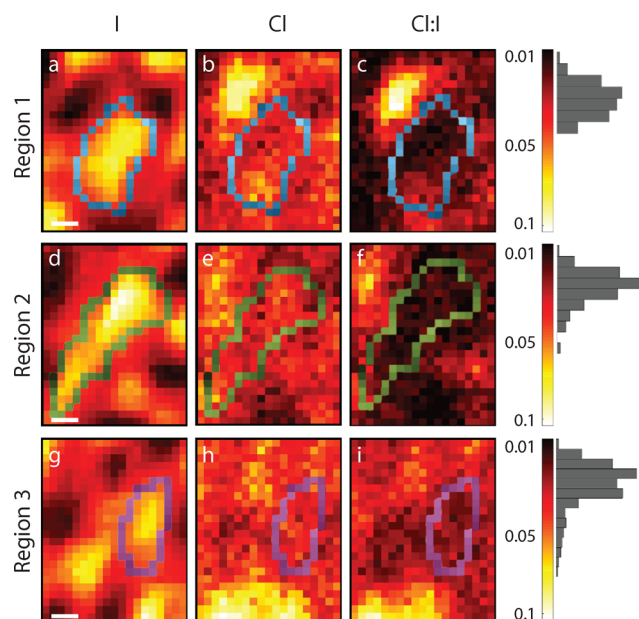


**Figure 6.** Three high-resolution images of regions of interest randomly selected from the Cl-containing  $\text{PbI}_2 + \text{MACl:MAI}$  (1:1, 1s) sample. The highlighted boundary indicates the approximate outline of a single particle. The Cl:I map visualizes the varying chemical distribution. Within each boundary, the Cl:I ratio is computed with a summary histogram shown next to the Cl:I color bar. Scale bar is 100 nm.

In optoelectronic materials and solar cells in particular, heterogeneous elemental distributions often lead to defective regions that are detrimental to performance, in part due to the consequence of local  $V_{\text{OC}}$  fluctuations particularly in heterojunction or organic solar cells.<sup>49</sup> The effect of minor element incorporation and segregation to crystalline lattice defects such as grain boundaries depends strongly on the material system. A heterogeneous distribution of sodium has been shown to be beneficial and enhance efficiency of  $\text{Cu(In,Ga)Se}_2$  photovoltaics when incorporated along the grain boundaries.<sup>30</sup> Early indications in lead halide perovskite materials from spatially resolved photoluminescence measurements are that Cl may have a positive optoelectronic effect,<sup>7</sup> beyond crystal growth impacts. Cl segregation to interfaces between the device layers has also been demonstrated along the depth of the device by synchrotron-based X-ray photoelectron spectroscopy studies<sup>50</sup> and implicated in enhanced interfacial charge transport.<sup>22</sup>

The in-plane distribution indicates that Cl-rich areas appear adjacent to the boundary of some particles, perhaps indicating spatial segregation (Figure 3i–l, Figure 6). The heterogeneous Cl incorporation observed here may lead to electrostatic effects at grain boundaries, such as (1) wider bandgap  $\text{MAPbCl}_3$  blocking layers that prevent minority carriers from reaching recombination sites at the grain boundary or perhaps (2) enhancing performance by acting as current-collecting channels as is the case of trace Cl in CdTe solar cells.<sup>51</sup> The nanoscale variations in Cl content that are directly observed here correspond to recent observation of local, nanoscale variations in bandgap in  $\text{CH}_3\text{NH}_3\text{PbI}_{3-x}\text{Cl}_x$  films by Chae et al.<sup>26</sup> that were attributed to the heterogeneity of a Cl-doped perovskite phase. The spatial segregation of Cl seen may suggest a preferential heterojunction band alignment forms at grain boundaries, enhancing device performance by limiting recombination. Similarly, scanning Kelvin-probe force microscopy has found potential differences across grain boundaries

relative to the grain interior, possibly due to  $\text{PbI}_2$  phase segregation at grain boundaries.<sup>52,53</sup> However, other Kelvin-probe force microscopy studies of grain boundaries in  $\text{CH}_3\text{NH}_3\text{I}_{3-x}\text{Cl}_x$  films reveal insignificant potential variation across the bulk or at boundaries, suggesting that no depletion region develops at these interfaces.

Using Cl-containing precursors has been shown to produce longer bulk lifetimes<sup>2</sup> and faster charge transfer to carrier transport layers.<sup>22</sup> Instead of electrostatic impacts, it may be that (3) the heterogeneous distribution of Cl may contribute to chemical passivation of defect and interface states. Further work is required to elucidate the Cl content and distribution after various annealings to deconvolute the optoelectronic role of Cl.

To the extent that Cl plays a role in improving electronic quality, the high degree of in-plane spatial variation in Cl incorporation in perovskite thin films evidenced here may be partially responsible for the generally large variation seen in final device performance<sup>55</sup> and may contribute to the difficulty in scaling highly efficient devices to larger areas.<sup>56</sup> The degree of heterogeneity may be reduced by extended annealing, as indicated in Cl-containing films<sup>26</sup> and mixed bromide-iodide lead perovskite film from 1s deposition.<sup>57</sup> Future work is needed to obtain high resolution, large-area correlative microscopy of the local electronic performance and remnant Cl distribution in the bulk of grains and at their boundaries. The distribution of chlorine may need to be controlled within the bulk of the perovskite particles and also tailored at the crystal boundaries and interfaces to produce robust, highly functional devices with tight performance distributions.

## CONCLUSIONS

Synchrotron-based X-ray fluorescence nanoprobe microscopy provides direct quantification of the degree of Cl incorporation in lead halide perovskite materials, with demonstration of local variations in Cl content with 100 nm resolution. Cl is positively identified within perovskite absorber materials synthesized by two-step, one-step, and spray deposition methods. By varying the amount of Cl in the perovskite precursors, the area-averaged Cl incorporation can be altered by nearly a factor of 2 in methylammonium lead halide perovskite film stacks. However, the Cl spatial distribution within a given film is highly heterogeneous. Variation in Cl content within single particles can approach the total variation measured in the film. Cl-rich regions are observed along or adjacent to crystal grain boundaries. Future work is required to determine Cl distribution dependency on deposition technique, annealing condition, and the resulting morphology. Control over the chlorine distribution may provide a path to significant performance and stability improvement by realizing uniform lifetime and charge transfer benefits.

## ASSOCIATED CONTENT

### Supporting Information

The Supporting Information is available free of charge on the ACS Publications website at DOI: 10.1021/acs.chemmater.6b02065.

X-ray beam resolution determination, crystal XRD measurement, film stability illustration under hard X-ray beam, and film attenuation correction (PDF)



## ■ AUTHOR INFORMATION

## Corresponding Author

\*Tel: (858) 246-0864; E-mail: [dfenning@ucsd.edu](mailto:dfenning@ucsd.edu) (D.P.F.).

## Notes

The authors declare no competing financial interest.

## ■ ACKNOWLEDGMENTS

The authors gratefully acknowledge Peter Fuesz's experimental assistance at the beamline, and Yang Shao-Horn's helpful support and discussions. Y.L. acknowledges the support of the UC Carbon Neutrality Initiative and DPF start-up funds from the University of California, San Diego. L.E. acknowledges the Tashtiot Project of the Office of the Chief Scientist, and the German Israel Foundation for Young Researchers. This research used resources of both the Center for Nanoscale materials and the Advanced Photon Source, a U.S. Department of Energy (DOE) Office of Science User Facility operated for the DOE Office of Science by Argonne National Laboratory under Contract No. DE-AC02-06CH11357.

## ■ REFERENCES

- (1) Wang, Y.; Gould, T.; Dobson, J. F.; Zhang, H.; Yang, H.; Yao, X.; Zhao, H. Density Functional Theory Analysis of Structural and Electronic Properties of Orthorhombic Perovskite  $\text{CH}_3\text{NH}_3\text{PbI}_3$ . *Phys. Chem. Chem. Phys.* **2014**, *16*, 1424–1429.
- (2) Stranks, S. D.; Eperon, G. E.; Grancini, G.; Menelaou, C.; Alcocer, M. J. P.; Leijtens, T.; Herz, L. M.; Petrozza, A.; Snaith, H. J. Electron-Hole Diffusion Lengths Exceeding. *Science* **2013**, *342*, 341–345.
- (3) Shi, D.; Adinolfi, V.; Comin, R.; Yuan, M.; Alarousu, E.; Buin, A.; Chen, Y.; Hoogland, S.; Rothenberger, A.; Katsiev, K.; Losovyj, Y.; Zhang, X.; Dowben, P. A.; Mohammed, O. F.; Sargent, E. H.; Bakr, O. M. Low Trap-State Density and Long Carrier Diffusion in Organolead Trihalide Perovskite Single Crystals. *Science* **2015**, *347*, 519–522.
- (4) Tan, Z.-K.; Moghaddam, R. S.; Lai, M. L.; Docampo, P.; Higler, R.; Deschler, F.; Price, M.; Sadhanala, A.; Pazos, L. M.; Credgington, D.; Hanusch, F.; Bein, T.; Snaith, H. J.; Friend, R. H. SI: Bright Light-Emitting Diodes Based on Organometal Halide Perovskite. *Nat. Nanotechnol.* **2014**, *9*, 1–6.
- (5) Xing, G.; Mathews, N.; Lim, S. S.; Yantara, N.; Liu, X.; Sabba, D.; Grätzel, M.; Mhaisalkar, S.; Sum, T. C. Low-Temperature Solution-Processed Wavelength-Tunable Perovskites for Lasing. *Nat. Mater.* **2014**, *13*, 476–480.
- (6) Chen, Q.; Zhou, H.; Hong, Z.; Luo, S.; Duan, H.-S.; Wang, H.-H.; Liu, Y.; Li, G.; Yang, Y. Planar Heterojunction Perovskite Solar Cells via Vapor Assisted Solution Process. *J. Am. Chem. Soc.* **2014**, *136*, 622–625.
- (7) deQuilettes, D. W.; Vorpahl, S. M.; Stranks, S. D.; Nagaoka, H.; Eperon, G. E.; Ziffer, M. E.; Snaith, H. J.; Ginger, D. S. Impact of Microstructure on Local Carrier Lifetime in Perovskite Solar Cells. *Science* **2015**, *348*, 683–686.
- (8) De Bastiani, M.; D'Innocenzo, V.; Stranks, S. D.; Snaith, H. J.; Petrozza, A. Role of the Crystallization Substrate on the Photoluminescence Properties of Organo-Lead Mixed Halides Perovskites. *APL Mater.* **2014**, *2*, 081509.
- (9) Park, N. G. Organometal Perovskite Light Absorbers Toward a 20% Efficiency Low-Cost Solid-State Mesoscopic Solar Cell. *J. Phys. Chem. Lett.* **2013**, *4*, 2423–2429.
- (10) Snaith, H. J. Perovskites: The Emergence of a New Era for Low-Cost, High-Efficiency Solar Cells. *J. Phys. Chem. Lett.* **2013**, *4*, 3623–3630.
- (11) Stranks, S. D.; Snaith, H. J. Metal-Halide Perovskites for Photovoltaic and Light-Emitting Devices. *Nat. Nanotechnol.* **2015**, *10*, 391–402.
- (12) NREL. Potential of Perovskite Solar Cells Featured in Solar Todaytitle <http://www.nrel.gov/pv/news/2016/21642.html>.
- (13) Christians, J. a.; Fung, R. C. M.; Kamat, P. V. An Inorganic Hole Conductor for Organo-Lead Halide Perovskite Solar Cells. Improved Hole Conductivity with Copper Iodide. *J. Am. Chem. Soc.* **2014**, *136*, 758–764.
- (14) Noh, J. H.; Im, S. H.; Heo, J. H.; Mandal, T. N.; Seok, S. I. Chemical Management for Colorful, Efficient, and Stable Inorganic-Organic Hybrid Nanostructured Solar Cells. *Nano Lett.* **2013**, *13*, 1764–1769.
- (15) Edri, E.; Kirmayer, S.; Cahen, D.; Hodes, G. High Open-Circuit Voltage Solar Cells Based on Organic – Inorganic Lead Bromide Perovskite. *J. Phys. Chem. Lett.* **2013**, *4*, 897–902.
- (16) Docampo, P.; Ball, J. M.; Darwich, M.; Eperon, G. E.; Snaith, H. J. Efficient Organometal Trihalide Perovskite Planar-Heterojunction Solar Cells on Flexible Polymer Substrates. *Nat. Commun.* **2013**, *4*, 1–6.
- (17) Bi, D.; Yang, L.; Boschloo, G.; Hagfeldt, A.; Johansson, E. M. J. Effect of Different Hole Transport Materials on Recombination in  $\text{CH}_3\text{NH}_3\text{PbI}_3$  Perovskite-Sensitized Mesoscopic Solar Cells. *J. Phys. Chem. Lett.* **2013**, *4*, 1532–1536.
- (18) Tidhar, Y.; Edri, E.; Weissman, H.; Zohar, D.; Cahen, D.; Rybtchinski, B.; Kirmayer, S. Crystallization of Methyl Ammonium Lead Halide Perovskites: Implications for Photovoltaic Applications. *J. Am. Chem. Soc.* **2014**, *136*, 13249–13256.
- (19) Zhao, Y.; Zhu, K.  $\text{CH}_3\text{NH}_3\text{Cl}$ -Assisted One-Step Solution Growth of  $\text{CH}_3\text{NH}_3\text{PbI}_3$ : Structure, Charge-Carrier Dynamics, and Photovoltaic Properties of Perovskite Solar Cells. *J. Phys. Chem. C* **2014**, *118*, 9412–9418.
- (20) Unger, E. L.; Bowring, A. R.; Tassone, C. J.; Pool, V. L.; Goldparker, A.; Checharoen, R.; Stone, K. H.; Hoke, E. T.; Toney, M. F.; McGehee, M. D. Chloride in Lead Chloride-Derived Organo-Metal Halides for Perovskite-Absorber Solar Cells. *Chem. Mater.* **2014**, *26*, 7158–7165.
- (21) Yu, H.; Wang, F.; Xie, F.; Li, W.; Chen, J.; Zhao, N. The Role of Chlorine in the Formation Process of “ $\text{CH}_3\text{NH}_3\text{PbI}_{3-x}\text{Cl}_x$ ” Perovskite. *Adv. Funct. Mater.* **2014**, *24*, 7102–7108.
- (22) Chen, Q.; Zhou, H.; Fang, Y.; Stieg, A. Z.; Song, T.-B.; Wang, H.-H.; Xu, X.; Liu, Y.; Lu, S.; You, J.; Sun, P.; McKay, J.; Goorsky, M. S.; Yang, Y. The Optoelectronic Role of Chlorine in  $\text{CH}_3\text{NH}_3\text{PbI}_3(\text{Cl})$ -Based Perovskite Solar Cells. *Nat. Commun.* **2015**, *6*, 1–9.
- (23) Wang, Q.; Lyu, M.; Zhang, M.; Yun, J.-H.; Chen, H.; Wang, L. Transition from Tetragonal to Cubic Phase of Organohalide Perovskite: The Role of Chlorine in Crystal Formation of  $\text{CH}_3\text{NH}_3\text{PbI}_3$  on  $\text{TiO}_2$  Substrates. *J. Phys. Chem. Lett.* **2015**, *6*, 4379–4384.
- (24) Dar, M. I.; Arora, N.; Gao, P.; Ahmad, S.; Gratzel, M.; Nazeeruddin, M. K. Investigation Regarding the Role of Chloride in Organic-Inorganic Halide Perovskites Obtained from Chloride Containing Precursors. *Nano Lett.* **2014**, *14*, 6991–6996.
- (25) Pool, V. L.; Gold-Parker, A.; McGehee, M. D.; Toney, M. F. Chlorine in  $\text{PbCl}_2$ -Derived Hybrid-Perovskite Solar Absorbers. *Chem. Mater.* **2015**, *27*, 7240–7243.
- (26) Chae, J.; Dong, Q.; Huang, J.; Centrone, A. Chloride Incorporation Process in  $\text{CH}_3\text{NH}_3\text{PbI}_{3-x}\text{Cl}_x$  Perovskites via Nanoscale Bandgap Maps. *Nano Lett.* **2015**, *15*, 8114–8121.
- (27) Colella, S.; Mosconi, E.; Fedeli, P.; Listorti, A.; Orlandi, F.; Ferro, P.; Besagni, T.; Rizzo, A.; Calestani, G.; Gigli, G.; Angelis, F.; De Mosca, R.; Gazza, F.  $\text{MAPbI}_{3-x}\text{Cl}_x$  Mixed Halide Perovskite for Hybrid Solar Cells: The Role of Chloride as Dopant on the Transport and Structural Properties. *Chem. Mater.* **2013**, *25*, 4613–4618.
- (28) Liu, L.; Choi, H. W.; Lai, P. T.; Xu, J. Passivation of Oxide Traps in Gallium Arsenide (Semiconductor) Metal-Oxide-Semiconductor Capacitor with High-K Dielectric by Using Fluorine Incorporation. *J. Vac. Sci. Technol. B* **2015**, *33*, 1–5.
- (29) Sakurai, T. Theory of Continuously Distributed Trap States at Si-SiO<sub>2</sub> Interfaces. *J. Appl. Phys.* **1981**, *52*, 2889–2896.
- (30) Rudmann, D.; da Cunha, A. F.; Kaelin, M.; Kurdesau, F.; Zogg, H.; Tiwari, A. N.; Bilger, G. Efficiency Enhancement of  $\text{Cu}(\text{In,Ga})\text{Se}_2$

Solar Cells due to Post-Deposition Na Incorporation. *Appl. Phys. Lett.* **2004**, *84*, 1129–1131.

(31) Aberle, A. G. Overview on SiN Surface Passivation of Crystalline Silicon Solar Cells. *Sol. Energy Mater. Sol. Cells* **2001**, *65*, 239–248.

(32) Laban, W. A.; Etgar, L. Depleted Hole Conductor-Free Lead Halide Iodide Heterojunction Solar Cells. *Energy Environ. Sci.* **2013**, *6*, 3249–3253.

(33) Mei, A.; Li, X.; Liu, L.; Ku, Z.; Liu, T.; Rong, Y.; Xu, M.; Hu, M.; Chen, J.; Yang, Y.; Grätzel, M.; Han, H. A Hole-Conductor-free, Fully Printable Mesoscopic Perovskite Solar Cell with High Stability. *Science* **2014**, *345*, 295–298.

(34) Aharon, S.; Gamliel, S.; El Cohen, B.; Etgar, L. Depletion Region Effect of Highly Efficient Hole Conductor Free CH<sub>3</sub>NH<sub>3</sub>PbI<sub>3</sub> Perovskite Solar Cells. *Phys. Chem. Chem. Phys.* **2014**, *16*, 10512–10518.

(35) Cohen, B.-E.; Aharon, S.; Dymshits, A.; Etgar, L. Impact of Anti-Solvent Treatment on Carrier Density in Efficient Hole Conductor Free Perovskite Based Solar Cells. *J. Phys. Chem. C* **2016**, *120*, 142–147.

(36) Qiu, J.; Qiu, Y.; Yan, K.; Zhong, M.; Mu, C.; Yan, H.; Yang, S. All-Solid-State Hybrid Solar Cells Based on a New Organometal Halide Perovskite Sensitizer and One-Dimensional TiO<sub>2</sub> Nanowire Arrays. *Nanoscale* **2013**, *5*, 3245–3248.

(37) Cohen, B. E.; Gamliel, S.; Etgar, L. Parameters Influencing the Deposition of Methylammonium Lead Halide Iodide in Hole Conductor Free Perovskite-Based Solar Cells. *APL Mater.* **2014**, *2*, 1–8.

(38) Gamliel, S.; Dymshits, A.; Aharon, S.; Terkieltaub, E.; Etgar, L. Micrometer Sized Perovskite Crystals in Planar Hole Conductor Free Solar Cells. *J. Phys. Chem. C* **2015**, *119*, 19722–19728.

(39) Burschka, J.; Pellet, N.; Moon, S.-J.; Humphry-Baker, R.; Gao, P.; Nazeeruddin, M. K.; Grätzel, M. Sequential Deposition as a Route to High-Performance Perovskite-Sensitized Solar Cells. *Nature* **2013**, *499*, 316–320.

(40) Barrows, A.; Pearson, A.; Kwak, C.; Dunbar, A.; Buckley, A.; Lidzey, D. Efficient Planar Heterojunction Mixed-Halide Perovskite Solar Cells Deposited via Spray-Deposition. *Energy Environ. Sci.* **2014**, *7*, 2944–2950.

(41) Hubbell, J. H.; Seltzer, S. Tables of X-Ray Mass Attenuation Coefficients and Mass Energy-Absorption Coefficients (version 1.4) <http://physics.nist.gov/xaamdi>.

(42) Winarski, R. P.; Holt, M. V.; Rose, V.; Fuesz, P.; Carbaugh, D.; Benson, C.; Shu, D.; Kline, D.; Brian Stephenson, G.; McNulty, L.; Maser, J.; Stephenson, G. B.; McNulty, L.; Maser, J. A Hard X-Ray Nanoprobe Beamline for Nanoscale Microscopy. *J. Synchrotron Radiat.* **2012**, *19*, 1056–1060.

(43) GmbH, A. D. AXO DRESDEN GmbH [http://www.axo-dresden.de/products/AXO-Prospectus\\_web.pdf](http://www.axo-dresden.de/products/AXO-Prospectus_web.pdf).

(44) Vogt, S. MAPS: A Set of Software Tools for Analysis and Visualization of 3D X-Ray Fluorescence Data Sets. *J. Phys. IV* **2003**, *104*, 635–638.

(45) Mosconi, E.; Amat, A.; Nazeeruddin, M. K.; Grätzel, M.; De Angelis, F. First-Principles Modeling of Mixed Halide Organometal Perovskites for Photovoltaic Applications. *J. Phys. Chem. C* **2013**, *117*, 13902–13913.

(46) Ball, J. M.; Lee, M. M.; Hey, A.; Snaith, H. J. Low-Temperature Processed Meso-Superstructured to Thin-Film Perovskite Solar Cells. *Energy Environ. Sci.* **2013**, *6*, 1739.

(47) Smith, I. C.; Hoke, E. T.; Solis-Ibarra, D.; McGehee, M. D.; Karunadasa, H. I. A Layered Hybrid Perovskite Solar-Cell Absorber with Enhanced Moisture Stability. *Angew. Chem.* **2014**, *126*, 11414–11417.

(48) Kaelin, M.; Rudmann, D.; Kurdesau, F.; Zogg, H.; Meyer, T.; Tiwari, A. N. Low-Cost CIGS Solar Cells by Paste Coating and Selenization. *Thin Solid Films* **2005**, *480*, 486–490.

(49) Luria, J. L.; Hoepker, N.; Bruce, R.; Jacobs, A. R.; Groves, C.; Marohn, J. a. Spectroscopic Imaging of Photopotentials and Photoinduced Potential Fluctuations in a Bulk Heterojunction Solar Cell Film. *ACS Nano* **2012**, *6*, 9392–9401.

(50) Starr, D. E.; Sadoughi, G.; Handick, E.; Wilks, R. G.; Alseimer, J. H.; Köhler, L.; Gorgoi, M.; Snaith, H. J.; Bär, M. Direct Observation of an Inhomogeneous Chlorine Distribution in CH<sub>3</sub>NH<sub>3</sub>PbI<sub>3-x</sub>Cl<sub>x</sub> Layers: Surface Depletion and Interface Enrichment. *Energy Environ. Sci.* **2015**, *8*, 1609–1615.

(51) Li, C.; Wu, Y.; Poplawsky, J.; Pennycook, T. J.; Paudel, N.; Yin, W.; Haigh, S. J.; Oxley, M. P.; Lupini, A. R.; Al-Jassim, M.; Pennycook, S. J.; Yan, Y. Grain-Boundary-Enhanced Carrier Collection in CdTe Solar Cells. *Phys. Rev. Lett.* **2014**, *112*, 1–5.

(52) Yun, J. S.; Ho-Baillie, A.; Huang, S.; Woo, S. H.; Heo, Y.; Seidel, J.; Huang, F.; Cheng, Y. B.; Green, M. A. Benefit of Grain Boundaries in Organic-Inorganic Halide Planar Perovskite Solar Cells. *J. Phys. Chem. Lett.* **2015**, *6*, 875–880.

(53) Chen, Q.; Zhou, H.; Song, T.; Bin Luo, S.; Hong, Z.; Duan, H. S.; Dou, L.; Liu, Y.; Yang, Y. Controllable Self-Induced Passivation of Hybrid Lead Iodide Perovskites toward High Performance Solar Cells. *Nano Lett.* **2014**, *14*, 4158–4163.

(54) Edri, E.; Kirmayer, S.; Mukhopadhyay, S.; Gartsman, K.; Hodes, G.; Cahen, D. Elucidating the Charge Carrier Separation and Working Mechanism of CH<sub>3</sub>NH<sub>3</sub>PbI<sub>3-x</sub>Cl<sub>x</sub> Perovskite Solar Cells. *Nat. Commun.* **2014**, *5*, 1–8.

(55) Malinkiewicz, O.; Yella, A.; Lee, Y. H.; Espallargas, G. M. M.; Graetzel, M.; Nazeeruddin, M. K.; Bolink, H. J. Perovskite Solar Cells Employing Organic Charge-Transport Layers. *Nat. Photonics* **2013**, *8*, 128–132.

(56) Hodes, G.; Cahen, D. Photovoltaics Perovskite Cells Roll Forward. *Nat. Photonics* **2014**, *8*, 87–88.

(57) Sadhanala, A.; Deschler, F.; Thomas, T. H.; Dutton, S. E.; Goedel, K. C.; Hanusch, F. C.; Lai, M. L.; Steiner, U.; Bein, T.; Docampo, P.; Cahen, D.; Friend, R. H. Preparation of Single Phase Films of CH<sub>3</sub>NH<sub>3</sub>Pb(I<sub>1-x</sub>Br<sub>x</sub>)<sub>3</sub> with Sharp Optical Band Edges. *J. Phys. Chem. Lett.* **2014**, *5*, 2501–2505.